Microstructure and magnetization evolution in bcc iron via direct first-principles predictions of radiation effects

Ebrahim Mansouri [*] and Pär Olsson [†]
KTH Royal Institute of Technology, Nuclear Engineering, Roslagstullsbacken 21, 114 21 Stockholm, Sweden

(Received 6 September 2023; accepted 15 November 2023; published 21 December 2023)

We here model the radiation-induced microstructure evolution in bcc iron using the creation-relaxation algorithm directly driven by density functional theory calculations and compare to interatomic potential simulations. The method is in essence a relatively simplified model without thermally driven diffusion. The microstructure evolution in this model is driven mostly by the stress field introduced by sequential direct damage insertions. The defect populations and the corresponding defect cluster characteristics have been analyzed as a function of irradiation dose. Different distribution functions have been investigated for the self-interstitial atom implantation, to make model predictions as close as possible to actual irradiation conditions under which defects are produced. The stability and magnetic characteristics of the defect structures that are formed are studied. Our first-principles simulations revealed that the C15 structure can be dynamically formed during the irradiation of the material and that the constituent atoms align antiferromagnetically to the lattice. For doses on the order of a fraction of 1 displacement per atom, the model material Fe experiences mechanical changes caused by continuous irradiation and approaches a saturation state of about 2% swelling. The radiation-induced change in the local magnetic moments as well as the charge density differences for some isolated and clustered defects have been investigated. The results revealed a net reduction in total magnetization per atom and a tendency for interstitial sites to have a spin polarization opposing the intrinsic atomic site spins when the coordination number was increased compared to that of the initial lattice structure. It is suggested that radiation-induced damage could be traced using nondestructive measures of bulk magnetization changes.

DOI: 10.1103/PhysRevMaterials.7.123604

I. INTRODUCTION

With emerging Generation IV nuclear reactors and future fusion reactor systems, it is required to develop different alloys whose in-reactor mechanical properties are expected to be more robust due to more aggressive environments than in current nuclear reactors [1]. During the operating lifetime of nuclear reactors, structural materials are constantly exposed to radiation in the form of energetic particles of various kinds, creating isolated point defects (i.e., vacancies and self-interstitials) and significant concentrations of extended defect clusters [2,3]. Upon accumulation of these irradiation-induced defects and clusters, complex microstructural segments are formed, including voids, dislocation loops, radiation-enhanced or induced solute segregation in alloys, and precipitation of secondary phases [4–6]. The microstructural evolution can cause significant changes in the physical and mechanical properties of the materials. Hardening, embrittlement, and dimensional changes such as creep, growth, and swelling are typical examples of macroscopic effects of irradiation [2,7,8]. Subsequently, alloys with high resistance to the adverse effects of irradiation are of great technological interest especially for the nuclear energy sector.

Indicating and exploring the long-term evolution of the microstructures and their associated physical property changes under irradiation conditions are complex and demanding tasks. Consequently, many studies and research programs have been conducted to investigate the effects of irradiation on the physical and mechanical properties of real or model materials [9–14]. Due to the limitation of nanoscale analysis capabilities, the experimental observations of irradiation-induced microstructure evolution remain relatively rare at the atomic scale [15]. Therefore, multiscale modeling approaches have been extensively developed to facilitate elucidating the relationship between microstructure evolution and physical property changes of irradiated material in recent years [5,13,16–18].

For example, Domain *et al.* applied the object kinetic Monte Carlo (OKMC) method to investigate the dynamics of the thermally activated microstructure evolution in Fe and FeCu alloys [19] for irradiation doses far below 1 displacement per atom (dpa).[1] Indeed, their study was relevant for reactor pressure vessel steels in light water reactors where

[*]Corresponding author: ebrman@kth.se
[†]Corresponding author: polsson@kth.se

[1]Displacement per atom (dpa) is a dimensionless positive-definite parameter that can be used to measure irradiation exposure [20]. As described by Kinchin and Pease [21] and quantified by Norgett *et al.* [22], atomic displacement is expressed by a dpa parameter φ.

the density of the defects is relatively low, and the lifetime dose is well below 1 dpa. Nevertheless, applying the OKMC approach to dose limits higher than 1 dpa, where the concentrations of isolated and extended defects are relatively high, e.g., in materials near the reactor cores, has so far proved problematic due to the high computational cost of modeling an environment with both slowly and rapidly diffusing defects, continuously created during operation. Furthermore, to improve the OKMC predictions even further, incorporation of both linear and nonlinear elastic interactions between almost all kinds of simple and complex defects are necessary but challenging [23,24]. Therefore, to model the microstructure evolution, there has been quite some activity focusing on directly applying interatomic potentials and molecular dynamics (MD) simulations over the past few decades [14,25,26], with different levels of assumptions and approximations included.

Granberg *et al.* applied the MD method to study defect accumulation and evolution in Fe-based alloys [27] and tungsten [25] using massive amounts of overlapping cascade simulations at room temperature. They generated isolated and extended defects through primary knock-on atoms induced by random initiation of thousands of subsequent displacement cascade events at room temperature. The time between the events is orders of magnitude shorter than the realistic one in representative conditions. While this method neglects many diffusion-driven events and mechanisms, an equivalent dose of 0.12 dpa was achieved in Fe and FeCr alloys [27]. Despite successfully reproducing the microscopic dynamics of atomic collisions under massive overlapping cascades, it was difficult to uncover the intermediate stages of defect evolution, as discussed by Derlet and Dudarev in Ref. [26].

Since the late 1980s, a simple yet powerful computational simulation technique was introduced by Limoge *et al.* for studying the irradiation-induced amorphization in noncrystalline materials by successive introduction of point defects, either Frenkel pairs (FPs) or isolated interstitials [28]. The approach has been widely adopted and adapted by various researchers over the past decades [29–32]. For instance, Derlet and Dudarev reformulated and integrated it with interatomic potentials and molecular statics, to explore the radiation-induced microstructure evolution of two model materials, Fe and W [26]. They successively introduced a FP defect consisting of a vacancy and self-interstitial atom (SIA) into a simulation cell through random selection and displacement of lattice atoms. After the defect was inserted, the atomic positions were relaxed to their local energy minima to track the accumulation of defects and their evolution at zero temperature, where the microstructure evolves solely as a result of the induced stress field from continuous FP insertions (FPIs). This process, named as the creation-relaxation algorithm (CRA), allows one to demonstrate the development of microstructure imperfections over several stages, including a linear accumulation of point defects ($\varphi \sim 0.01$ dpa), formation of interstitial clusters ($\varphi \sim 0.1$ dpa), creeping formation of dislocation loops (0.7 dpa), and finally saturation of the dislocation network ($\varphi \sim 1.5$ dpa).

Given that the CRA model ignores the high-energy characteristics of defect production, it addresses one of the significant challenges for OKMC simulations by directly considering linear and nonlinear lattice deformations caused by defect accumulations. In contrast to overlapping cascade simulations, the CRA model significantly reduces the computational effort by neglecting the high-energy stages of radiation damage production, allowing for the exploration of high dose values (e.g., up to 2.5 dpa and beyond) in larger simulation cells. Thus, the CRA model identifies the stages of isolated and extended defect accumulation and demonstrates microstructure evolution into a final steady-state structure at high dose levels without thermal activation.

Before the CRA model was introduced, Chartier and Marinica [29] employed a similar technique to study the interactions between dislocations and small C15 Laves phase inclusions, with an icosahedral structure, in the body-centered cubic (bcc) Fe structure under irradiation conditions. They applied an embedded-atom method (EAM) potential, referred to as M07 [33], to simulate the formation of three-dimensional C15 clusters by accumulating FPs. Their findings revealed a complex interplay between two-dimensional interstitial defects ($1/2\langle 111\rangle$ and $\langle 100\rangle$ loops) and three-dimensional C15 clusters. However, using the Mendelev *et al.* EAM potential (M03) [34], Derlet observed minimal icosahedral content during the nucleation of the dislocation loop stage and therefore was unable to resolve other possible mixed Laves C15/dislocation loop structures. The study highlighted differences in observed structures, indicating that the choice of interatomic potentials may account for these disparities. In fact, the M03 potential used in Ref. [26] is a quite energetically unfavorable potential for large C15 cluster formation, as shown in [35].

Furthermore, both studies attribute the generation of damage to electron irradiation under low-temperature conditions, which predict the production of FPs. Moreover, the investigations conducted in both studies employed relatively large supercells with side lengths exceeding $80 \times a_0$,[2] allowing for a large displacement and uniform distribution of SIAs. However, it should be noted that this uniform distribution of implanted SIAs, though it simplifies the simulation, may introduce an unrealistic assumption on the mean free path of a dynamically created SIA in a newly born FP that could impact the nature of microstructure evolution during the initial stages of irradiation.

Finally, in this study, we propose a first-principles driven CRA model using density functional theory (DFT) for the simulation of defect production, energy minimization, and microstructure evolution. Consequently, by applying a DFT-driven CRA model, one can reproduce the radiation-induced microstructure evolution while resolving the evolving electronic structure and tracing its effects, with additional value in detailed information on aspects such as local and global magnetization and charge density evolution, as well as the potential to expand to complex alloys without loss of quality in the physical description. Indeed, the DFT method provides a solid benchmark to validate the results achieved by using interatomic potentials. It also provides a tool to investigate the possible effects of radiation-induced microstructure on the quenching and polarization of local magnetic moments and

[2] a_0 is referred to as the lattice parameter.

charge density difference distributions around isolated defects and defect clusters, e.g., C15-type clusters. In contrast to the aforementioned studies based on a semiempirical potential drive CRA that utilized large supercells, our study employs a relatively small supercell ($8 \times a_0$ with 1024 atomic sites), eliminating the need to consider spatially localized or uniform SIA distributions within the simulation cell. To accurately model low-energy defect production, such as electron irradiation, it should be more appropriate to employ a locally distributed SIA implantation model in large supercells.

The current study is structured into three distinct sections. Section II describes the CRA model in detail and outlines the computational specifics. Section III delves into the discourse of the findings and provides a comprehensive discussion of the results. Subsequently, the study conclusion is presented in its dedicated section. Furthermore, in Appendix A, an explication of the forbidden zone radius (FZR) criterion is expounded upon. Appendix B elucidates the three distinct spatial distribution functions employed for SIA distributions. Finally, the Supplemental Material pertinent to this study are comprehensively detailed in [36].

II. METHODS

A. CRA

This study applied the CRA approach to directly generate Frenkel pairs, mimicking low-energy damage events, and to qualitatively simulate a bulk radiation dose and microstructural evolution in bcc Fe. Using the canonical definition of dpa [26], one may determine the irradiation dose by dividing the FPI number, n, by the total number of lattice sites, $N(\varphi = n/N)$. Considering the importance of the algorithm used in this study, as well as the slight differences we applied in our calculation requirements compared to those applied in Ref. [26], the CRA model is briefly reviewed and rewritten according to our simulation conditions:

(1) Construction of a simulation cell with N lattice sites of a desired size and crystallography.

(2) Determination of the radius of a forbidden zone; explained in Appendix A.

(3) Relaxation of the ionic positions in the cell before insertion and considering this cell as a reference configuration.

(4) Setting n to 0.

(5) Random selection and removal of an atom within the simulation cell, creating a vacancy.

(6) Insertion of the randomly selected atom into the simulation cell according to a selected distribution function, creating a SIA.

(7) Inspection whether the inserted atom is inside the forbidden zone of another atom and then conditional modification of its position to just outside the forbidden zone.

(8) Relaxation of all ionic positions by adopting an energy minimization method to find a new global potential energy minimum for all the atoms in the cell.

(9) Setting n to $n + 1$ and updating the value of the dose parameter φ to n/N.

(10) Iteration of steps (5)–(9) until the algorithm reaches the desired target dpa value.

Two main differences exist between our simulation requirements and those applied in [26]. For noticeably short distances, the empirical potentials in [26] are connected to the Ziegler, Biersack, and Littmark [37] screened Coulomb interaction. In this study, we only used a projector augmented wave description [38] with a minimal set of explicit valence electrons. Therefore, we are not guaranteed to achieve a fully appropriate short-range repulsive form, potentially leading to unreliable forces if the inserted atom is placed too close to another atom. Consequently, we defined a virtual spherical zone encompassing each atom within which the inserted atoms cannot be implanted before the relaxation step. If an atom is placed inside the forbidden zone of another atom due to the random coordinate selection, it is displaced directly outwards from the atom to the zone boundary, and from there, the relaxation starts. According to our calculations, this forbidden zone can be reasonably selected as about 0.7 Å in bcc Fe. In Appendix A, we have shown how this value has been assigned as a criterion for the forbidden zone radius. We can note that as long as the selected value is not too small (nonphysical forces) the resulting relaxation is quite stable with respect to the parameter value.

During energetic recoils initiated by an incoming particle, the spatial distribution of the resulting damage, be it in the form of cascade debris for high-energy impacts, or a distribution of isolated FPs, covers between a few angstrom up to a few nanometers. The characteristic size of the resulting distribution of defects scales very weakly with the energy of the incoming particle due to the many-body collision effects. Consequently, for modeling low-energy irradiation damage in large cells ($>10 \times a_0$ or so), especially within the CRA framework, the spatial distribution of the SIA implantation is critical for improving model prediction. In other words, when the recoil atoms are scattered in a realistic irradiation condition under low-energy defect production, such as in electron irradiation, their displacements typically range within a few lattice parameters. Therefore, to model low-energy irradiation conditions, it is more important to displace randomly selected atoms in accordance with a spatially localized distribution model, especially in large supercells compared to this range. Thus we applied three different spatial distributions of SIAs—a uniform random distribution and two nonuniform localized random distributions—according to which the SIAs are dispersed. In this way, we investigated whether the distribution of SIAs would lead to different microstructure evolutions. We could also prove that a uniform distribution of SIAs is a valid approach for small simulation cells. More details on the distribution functions can be found in Appendix B.

A PYTHON code was employed for damage creation and insertion. Additionally, PYTHON and OVITO [39] were used for analyzing the microstructure evolutions. A Wigner-Seits analysis implemented in OVITO was conducted to identify the remaining vacancy and SIAs in the simulation cells after the relaxation. For two defects to be considered as clustered together, cut-off criteria were set at the midpoint between the second and third nearest neighbor distances (3.5 Å) for vacancies and between the third and fourth nearest neighbor distances (4.1 Å) for SIAs, in accordance with literature [40,41]. Furthermore, considering that the C15 atoms have a distinctive icosahedral coordination, we apply the polyhedral template matching (PTM) analysis [42], with a

root-mean-square deviation value of 0.25, implemented in OVITO to recognize them.

B. *Ab initio* calculation details

The main focus of this study is to use electronic structure calculations in the framework of DFT for the energy minimization during the CRA direct damage insertion. We used the projector augmented plane wave method [38] implemented in the Vienna *ab initio* simulation package (VASP) [43]. The conjugate gradient method [44] was used to perform the energy minimization after every FPI [steps (5)–(9) of the CRA]. The exchange-correlation term was treated in the generalized gradient approximation, as parametrized by Perdew, Burke, and Ernzerhof [45,46]. All calculations were spin polarized, and periodic boundary conditions, along with the supercell approach, were employed. For the CRA modeling of radiation-induced microstructure evolution, we used a supercell of $8 \times 8 \times 8$ copies of the bcc orthogonal unit cell, comprised of 1024 atoms. For this relatively large supercell, the Brillouin zone was sampled by the gamma point in k space. To improve the prediction of the model and lower the statistical noise, we used four distinct CRA trajectories for each condition.

In our simulations, we utilized diverse degrees of freedom to steer the response of the irradiated system to FPIs. This governs how the system evolves under irradiation, including adjustments in ionic positions, simulation cell volume, and cell shape. For an evolving system under intense irradiation, full relaxation (relaxing ionic positions, volume, and shape of cell) calculation is ideal after each damage insertion. However, full relaxation demands significant computational resources in DFT. To address this, we limited the simulations to ionic relaxations, which adjusts only ionic positions while preserving the volume and shape of the supercell. Full relaxation was applied selectively in specific snapshots of a CRA trajectory, optimizing insights without introducing extensive computational costs.

For volume-conserving simulations, we employed a cut-off energy of 250 eV and a 1 meV energy convergence criterion for the self-consistent electronic loop. However, for fully relaxed calculations, we used a higher 350 eV cut-off energy to prevent volumetric changes from affecting energy and forces due to varying volume and included plane waves. To enhance accuracy, we reduced the energy minimization convergence criterion to 0.1 meV in this simulation set.

To explore irradiation-induced structural changes, two approaches can be employed. In the full relaxation calculation paradigm, tracking the supercell volume offers insights into volumetric changes. Alternatively, the ionic relaxation calculation method tracks hydrostatic pressure changes. Full relaxation achieves a global pressure convergence to zero, causing the supercell volume and shape to evolve, leading to explicit volumetric swelling in the case of FPIs. In contrast, fixed volume conditions allow estimation of radiation-induced swelling by relating the global hydrostatic pressure change (ΔP) to the bulk modulus (B), expressed as [47]

$$\frac{\Delta V}{V_0} = \frac{-\Delta P}{B}, \tag{1}$$

where $\Delta V/V_0$ is the relative volumetric change as a result of FPIs.

Using the DFT-CRA method, we also investigated the irradiation-induced change in the electronic charge distribution and in the global and local magnetization. Accordingly, isosurfaces depicting the variations in spin and charge densities surrounding those defects were computed using VESTA [48].

Additionally, for a more comprehensive analysis of variations in magnetization and charge density near isolated point defects, a series of supplementary calculations (see the Supplemental Material [36]) were conducted with higher accuracy in smaller supercells. Firstly, a supercell comprising $5 \times 5 \times 5$ copies of a bcc unit cell was used to separately calculate the induced change in magnetization and stress tensor components around a vacancy, SIA, or FP defects, respectively, with higher computational accuracy (denser Γ-centered $6 \times 6 \times 6$ k-point mesh and 350 eV cut-off energy). Secondly, the magnetovolume relationship [49] was examined in a standard ferromagnetic bcc Fe conventional unit cell with a denser k-point mesh of $11 \times 11 \times 11$ and 350-eV cut-off energy.

To explore the potential influence of atomic volume fluctuations induced by FPI on local magnetic moments, a Voronoi analysis was employed. This analysis, established using planes bisecting distances to atomic neighbors, was conducted using OVITO.

C. Interatomic potential calculation details

The EAM-CRA simulations that are directly comparable to the DFT-CRA results were performed in a supercell with side length of $8 \times a_0$ comprising 1024 atomic sites. The conjugate gradient method was used, and the simulations were performed with LAMMPS [50] to relax the structure and determine the new local potential energy minimum. In parallel to DFT, two distinct relaxation methods were used: one for simulations with fixed volume and another for simulations with fixed pressure.

To reduce statistical error and improve radiation-induced damage prediction, five CRA trajectory profiles were used. The EAM potentials of M03 and M07 were applied to model and investigate the atomic structure of Fe under irradiation within the CRA model.

III. RESULTS AND DISCUSSION

A. The evolution of energy and pressure changes with uniform and localized distribution of SIAs

We evaluated the reliability and accuracy of the EAM potentials used in this study by comparing to the predictions of the DFT-CRA method for prediction of radiation-induced microstructure evolution in terms of energy and pressure changes.

According to the definition of the canonical dpa [26], the FPI number divided by the number of lattice sites to achieve an irradiation dose of 1 dpa, 1024 FPs must be inserted into a supercell containing 1024 atomic sites. Using the EAM-CRA method, it is quite fast to reach doses of 1 dpa in such small supercells. For the DFT-CRA method, however, which involves a relatively large system of mutually interacting electrons and

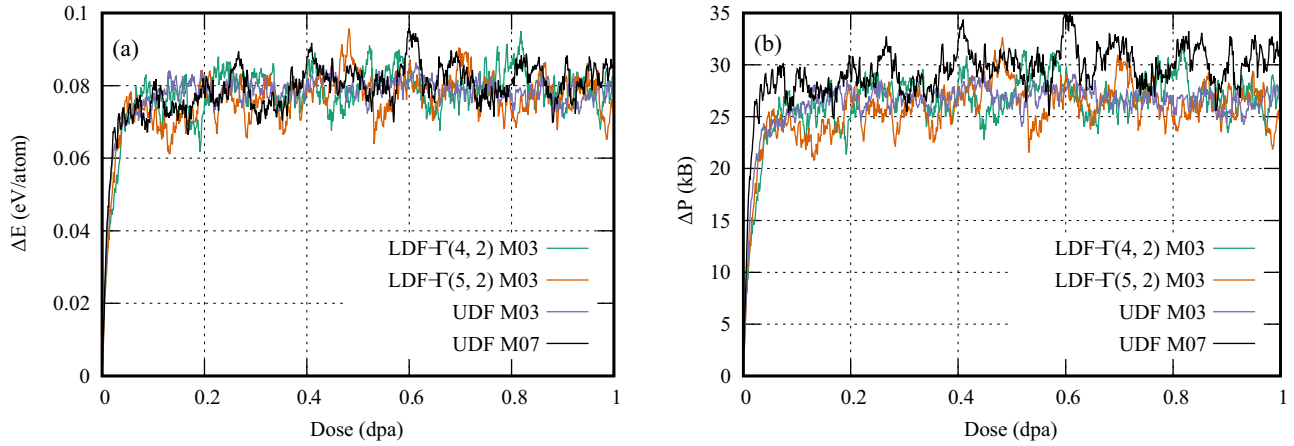

FIG. 1. Comparison of (a) energy change per atom and (b) hydrostatic pressure change as a function of FPI with different EAM-CRA methods.

ions, we stopped the simulation after 0.35 dpa since continuing the simulation to 1 dpa was not expected to yield much additional information.

First, the different SIA implantation distribution functions have been examined with the EAM-CRA model. As described in Appendix B, the mean displacement of the SIAs with a uniform distribution function (UDF) is about 11.3 Å in a supercell with the side length of $8 \times a_0$. In contrast, it is about 8 Å with a localized distribution function (LDF) such as the Γ(4,2) in the same supercell. Figure 1 compares the microstructure evolution of uniform and localized distributions of SIAs predicted by the EAM-CRA method, using different EAM potentials. Regardless of the type of spatial distribution of SIAs, the dose-dependent evolution of microstructure in the simulation cell is quite similar, as could be expected, given that the mean displacement of the SIAs is of the order of the simulation cell size. However, as mentioned earlier, in larger supercells ($> 10 \times a_0$), using a localized distribution of the SIAs would be logical if the objective is to simulate low-energy electron irradiation, which is one of the experimental conditions that the CRA model most closely resembles. From here on in this work, all results were obtained using the spatially uniform SIA implantation distribution within the supercells.

Figure 2 displays the change in total energy per atom (ΔE/atom) and the change in hydrostatic pressure (ΔP) as a function of dpa, extracted from the DFT-CRA and EAM-CRA methods. As shown, the EAM and DFT predictions are qualitatively comparable. Following an initial linear increase in both energy and pressure, a saturation stage develops after around 0.05 dpa, in agreement with earlier studies [26,27,40,51] (see Fig. S1 in [36]).

As shown in Fig. S1(a) in [36], regardless of the supercell size, the EAM-CRA model used in this study showed also entirely quantitative and qualitative agreement with the results reported in [26] in terms of ΔE/atom. However, depending on the size of the simulation cell, the pressure evolution [Fig. S1(b) in [36]] goes through at least three distinct stages. In summary, these stages include a rapid linear defect accumulation regime, a creeping dislocation loop formation stage, and a steady-state dislocation network formation stage [26,52,53]. As a result of using small supercells, large interstitial clusters and significant dislocation growth are not observed in this study. We see that in small supercells, only two stages of microstructure evolution are apparent: a quick linear accumu-

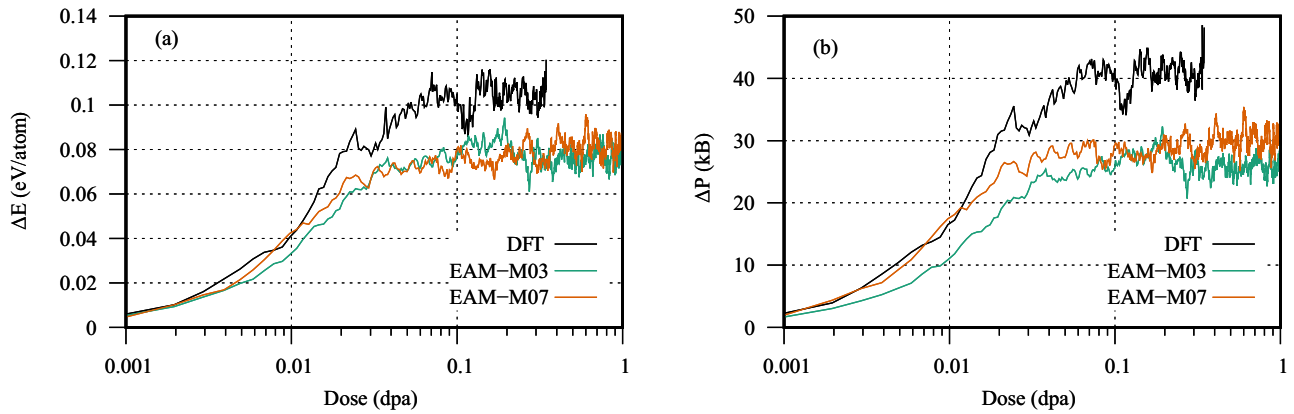

FIG. 2. Comparison of DFT and EAM estimating the average changes in (a) energy per atom and (b) global pressure as a function of dpa (FP insertion number divided by the number of lattice sites) in Fe.

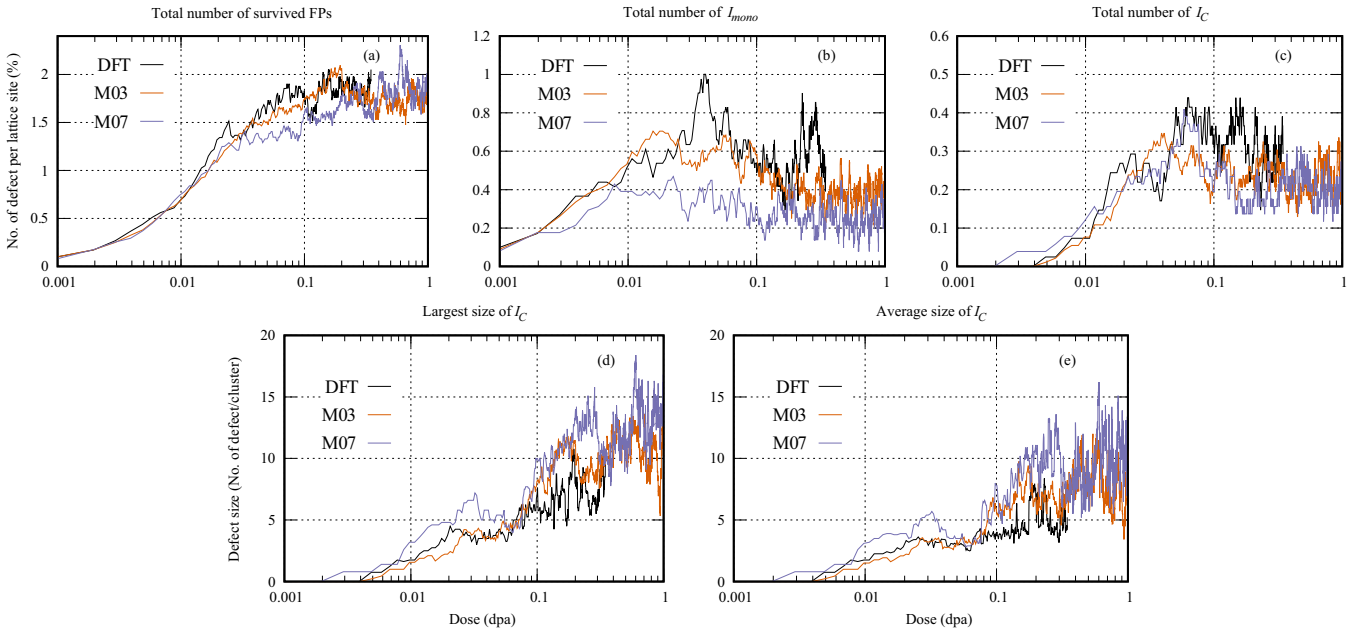

FIG. 3. Interstitial defect content per lattice site (top) and their cluster sizes (bottom) as a function of FP insertion (dpa) predicted by DFT, EAM-M03, and EAM-M07 methods.

lation of isolated point defects and a steady-state formation of small defect clusters, as also depicted in Fig. 2. Therefore, none of the DFT and EAM methods predicted the nucleation of stable dislocation loops in the supercell sizes used in this study, implying that the dislocation loops are unlikely to form out of the small interstitial clusters. The clusters must first grow larger or coalesce before they can merge into dislocation loops [26].

B. The evolution of the microstructure as a function of dose

The EAM potentials were further evaluated by comparing the microstructure evolution predicted by the DFT-CRA and EAM-CRA methods in terms of defect accumulation. Accordingly, we traced the defect populations and the cluster sizes, i.e., the total number of SIAs composing a cluster, as a function of irradiation dose. In addition, particular attention has been awarded to the irradiation-induced formation and evolution of three-dimensional C15 clusters.

Figure 3 shows the evolution of self-interstitial defect content per lattice site (top) and the cluster sizes (bottom) resulting from subsequent FP insertions in the model material Fe. As seen from the top graphs, the total number of survived FPs grows linearly for doses below 0.02 dpa and then stabilizes around a dose level of 0.05 dpa. Both the DFT and EAM methods qualitatively predict similarly evolving microstructures in Fe, within the conditions applied in this study. However, there is a statistically significant discrepancy between the DFT and EAM methods in estimating the number of isolated self-interstitial (I_{mono}) defects as well as the SIA cluster sizes. For example, the M07 potential overestimates the size of the interstitial cluster (I_C) by a factor of 2, while it estimates roughly half the number of I_{mono}, compared with the DFT results. This suggests that the M07 potential favors SIA cluster formation due to overstabilization.

Moreover, Fig. S2 in the Supplemental Material [36] compares the evolution of survived FPs predicted from different methodologies used in this study with those extracted from Ref. [26]. The number of survived FPs saturated at a dose of 0.05 dpa in supercells used in this study ($8 \times a_0$). Beyond 0.05 dpa, however, the number of survived FPs increases with a different linear slope using EAM-CRA, indicating nucleation and growth of dislocations in the sizable supercells used in Ref. [26]. In the present study, this evolution is only partly covered (up to about 0.2 dpa).

Although a qualitative similarity exists between the results of DFT and EAM simulations in predicting the microstructure evolution, for a thorough comparison of DFT versus EAM predictions, we determined the saturation-level average of several quantities (i.e., defect populations and their cluster sizes) from 0.05 dpa to the end of the irradiation dose and tabulated them in Table I. Accordingly, for the DFT results, the saturation level ranges from 0.05 to 0.35 dpa, while for the EAM data, it ranges from 0.05 to 1 dpa. In addition, the standard deviation, s_x, is also calculated for each quantity.

Table I shows that the DFT and EAM methodologies predict almost the same number of survived FPs. Moreover, the DFT-CRA method reveals that the number of survived isolated vacancies is roughly twice the number of isolated interstitial defects, even without the presence of dynamical bias. As shown in Table I and in the bottom graphs in Fig. S3 [36], the average and largest size of the interstitial clusters are significantly greater than those of the vacancy clusters. This suggests that the larger elastic strain field generated by SIAs leads to a stronger tendency to form a new structure phase, e.g., C15-type clusters as proposed by Dézerald *et al.* [54], rather than to remain as isolated point defects.

TABLE I. DFT and EAM predictions of the saturation level for defect populations and cluster sizes, along with their standard deviations (in parentheses). DFT data have been averaged over 0.05–0.35 dpa, whereas EAM data have been averaged over 0.05–1 dpa.

	Interstitial defect (s_x)			Vacancy defect (s_x)		
Method	DFT	EAM-M03	EAM-M07	DFT	EAM-M03	EAM-M07
No. of survived FP	18.6 (1.1)	18.0 (1.1)	18.2 (1.8)	18.6 (1.1)	18.0 (1.3)	18.2 (1.8)
No. of isolated defects	6.0 (1.3)	4.1 (0.8)	2.6 (0.7)	13.8 (1.3)	12.1 (0.9)	12.5 (1.5)
No. of defect clusters	3.2 (0.6)	2.4 (0.4)	2.1 (0.5)	2.2 (0.5)	2.4 (0.5)	2.4 (0.6)
Average size of the cluster[a]	4.6 (1.3)	7.3 (1.9)	9.4 (2.5)	2.0 (0.3)	2.2 (0.3)	2.3 (0.4)
Largest size of the cluster	6.8 (1.5)	10.0 (1.9)	12.1 (2.4)	2.2 (0.3)	2.6 (0.5)	2.6 (0.6)

[a]The defect cluster size equals the number of defects per cluster (No. defect/cluster).

A comparison between DFT and EAM predictions can also be identified from the bottom graphs in Fig. 3, showing the average and most significant cluster sizes of the SIAs. Despite similar qualitative trends, the EAM potentials imply that the average size of the interstitial clusters is roughly twice that of those anticipated by DFT simulations. It should be noted that these EAM potentials are based on DFT data but are not fitted on large defect clusters. Therefore, such discrepancies may be expected, and even later developed potentials relying on machine learning algorithms rarely include large variations of defect cluster energetics in their fitting database.

As mentioned earlier, the formation of nonparallel C15-type clusters has been already predicted to be energetically more favorable than other extended clusters in bcc Fe [35,54]. Using PTM analysis, we also traced the existence and formation of icosahedral structures to identify a possible formation of perfect or imperfect C15 Laves phase structures in our damaged bcc Fe cells. It is worth noting that clusters containing more than 12 SIAs are categorized as perfect C15 clusters, whereas those with fewer than 12 SIAs are classified as Laves phase backbone polyhedral structures or imperfect C15-type clusters. Figure 4 illustrates that the dose-dependent evolution of C15-type structures varies strongly depending on the methodology used for dose limits above 0.1 dpa where the average size of the interstitial clusters is larger than four SIAs.

Both DFT and EAM methods, regardless of the type of potential used, consistently predict the transformation of SIAs into C15-type clusters for doses below 0.1 dpa, where the average size of the interstitial clusters is smaller than four SIAs. However, our analysis revealed that above 0.1 dpa and up to the available DFT-driven irradiation dose of 0.35 dpa, where the formation of larger interstitial clusters is expected, the transformation of interstitial clusters into giant C15 structures is less frequent in irradiated bcc Fe when using the DFT method or the M03 potential compared to the M07 one. Therefore, the overall results obtained from the DFT and the EAM methods suggest that the M07 potential might overstabilize the formation of C15 clusters, in a more significant fashion than for SIA clusters in general, as was noted above. This result is expected, as the development of the M07 potential is based on the lower formation energy of three-dimensional C15 clusters, as suggested by *ab initio* calculations [35]. As also shown in Fig. 4, the frequent appearance of perfect C15 structures (clusters greater than 12 SIAs) is significant for the case of the M07 potential as compared to DFT and the M03 potential. It seems the dynamical evolution of complex cluster growth has not been fully captured by the potential fitting and that predictions using M07 may overestimate the prevalence of these clusters, at least in the simulation cells used in this study.

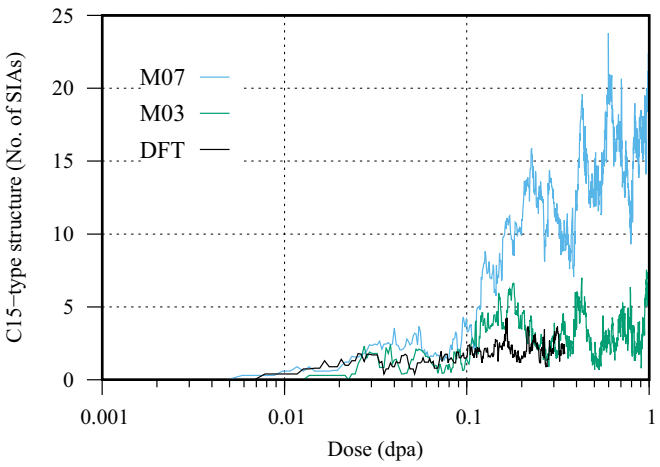

FIG. 4. The largest C15-type structures as a function of irradiation dose predicted by different methodologies.

As the predicted vacancy-related populations with either method or choice of EAM potential were compatible, we refrain from displaying them here. Instead, additional analysis of evolving vacancies and their clusters are provided in the Supplemental Material [36], Figs. S3 and S4. Those two graphs describe the evolution of vacancy-related defect populations and compare them with interstitial-related defects predicted by DFT and EAM potentials.

C. Radiation-induced structural change

Another way of studying the microstructure evolution is to trace the average change in physical properties such as the lattice constant and in volume expansion, i.e., swelling. Using the DFT- and EAM-CRA methods, we estimated the extent to which the model material Fe may experience radiation-induced volume expansion within the limit of the CRA conditions.

Referring to Eq. (1), we calculated the swelling using two different approaches. From the fixed volume CRA simulations, one can estimate the equivalent volumetric swelling by dividing the evolving global hydrostatic pressure by the appropriate bulk modulus (i.e., $\Delta P/B$) [47], as shown in Fig. 5. In addition, to directly determine the evolution of volumetric expansion, we fully relaxed the simulation cells

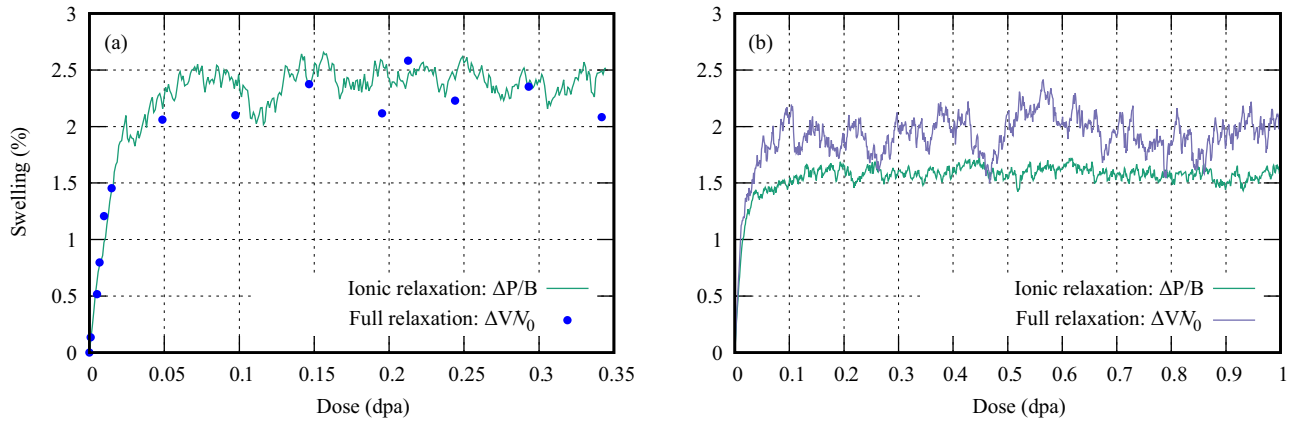

FIG. 5. A comparison of the (a) DFT and (b) EAM predictions of radiation-induced swelling with ionic and full relaxation calculations. Data points on DFT graphs correspond to snapshots taken from full relaxation calculation trajectory.

in several snapshots of a DFT-CRA trajectory. Due to the time-consuming nature of the full relaxation calculation in DFT the selected number of such snapshots was quite limited. In the full relaxation calculations, with cut-off energy 250 eV, we found that the explicit swelling ($\Delta V/V_0$) is approximately 30% lower than that predicted from ionic relaxation ($\Delta P/B$) calculations (see Fig. S5 in [36]). This apparent discrepancy is in part due to the low cut-off energy used for the full relaxation calculations which, given that the simulation cell undergoes volumetric expansion, changes the number of plane waves included in the expansion. To resolve this, we expanded the cut-off energy to 350 eV. As shown in Fig. 5, by doing so, the estimated swelling by ionic relaxation, with 250 eV cut-off energy, well resembled the directly calculated volumetric expansion, $\Delta V/V_0$, with 350 eV cut-off energy. It is worth noting that the results of full relaxation calculation with DFT are more closely matched to the fixed pressure calculation with EAM methods.

Similar structural changes have been reported in a 490 keV self-ion irradiation of 200 nm and 60 nm thick Fe films at room temperature [55,56], respectively. The lattice constant and the grain sizes, as measured by the grazing incidence x-ray diffraction technique, have been reported to initially undergo an abrupt increase at the early stage of irradiation and finally to a slow saturating steady state, similar to what we qualitatively predicted from our CRA model [see Figs. 5 and S6(a) [36]]. It has also been found that the bcc crystalline structure remains present and stable even after the high irradiation dose of 341 dpa. Our PTM analysis [Fig. S6(b)] in [36] also revealed that about 70% of the bcc structure still remains in the saturation stage of the damaged structure, within the CRA conditions.

D. Radiation-induced change in global and local magnetism

One of the extraordinary advantages of the DFT method over EAM simulations is that it allows one to study the possible magnetic transformation of a damaged structure, which cannot be accessed by means of classical EAM simulations. Herein, the irradiation-induced changes in global and local magnetization of the damaged bcc structures are investigated using the DFT-CRA model with ionic and full relaxation calculations. We first considered the evolution of the global magnetization (M) per atom as a function of dose in the supercells with the side length of $8 \times a_0$. In the early stage of FPIs, as shown in Fig. 6, the M decreases linearly with increasing irradiation dose. Upon reaching the saturation level (0.05 dpa), the total M fluctuates around 2.1 μ_B/atom as the number of survived FPs stabilizes.

Although making a direct correlation between the outcomes yielded by DFT calculations in absolute temperature and the findings gathered from experimental studies at room temperature might not be entirely suitable, yet qualitatively speaking, it is noteworthy that reductions in both total M and lattice parameter have been documented in recent investigations involving a 490 keV self-ion irradiation of 200 nm Fe films (composed of two top and bottom sublayers) at room temperature [55]. As mentioned by the author, the responses of those two sublayers seems to link to the impacts of Fe^+ irradiation: the top layer corresponded to regions primarily affected by irradiation damage, while the bottom layer pertained to both Fe^+ ion implantation and irradiation damage. As a result, the top Fe sublayer exhibited a higher magnetic moment than that of the unirradiated Fe sample whereas the bottom sublayer exhibited a lower average magnetization. In comparison with our simulation results, where magnetization

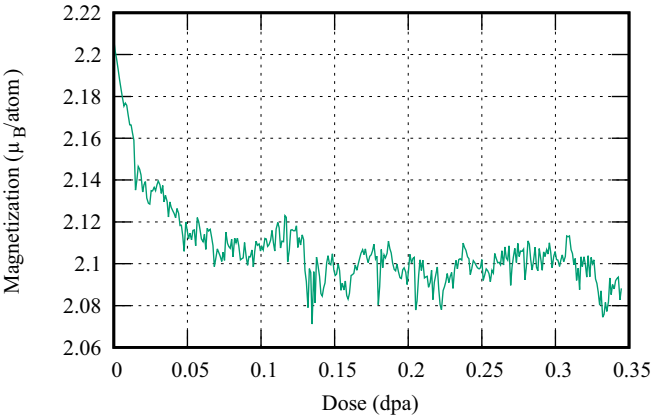

FIG. 6. The average magnetization per atom as a function of dose.

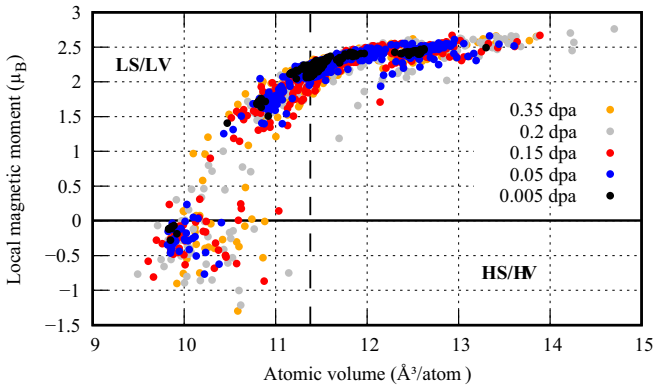

FIG. 7. Local magnetic moments of all atoms in different FPI stages for different irradiation dose levels, as a function of atomic volume. The vertical dashed line distinguishes LS/LV and HS/HV regions, highlighting deviations in atomic volume and local magnetic moments of atoms in the damaged bcc Fe structure with respect to the undamaged one.

is strictly decreasing with irradiation dose, the bottom layer evolution resembles this more. It is natural that a region with a higher SIA content will experience a quenching of magnetization, given both the decrease in average available free volume where there is a surplus of self-interstitials as well as the well-known strong direct magnetic quenching effects on SIAs themselves. For the top layer, the experimental result is, however, not in qualitative agreement with our results. An irradiated magnetic bulk material should not experience a growing magnetization, unless the swelling, and thus magnetovolume effect, can dominate over the defect-induced quenching. That we are simulating a perfect bulk, and the top layer is a thin substrate with a free surface may be part of the explanation of the discrepancy.

As explained in Sec. VII in the Supplemental Material [36], there is a net decrease of $1.72\,\mu_B$ (equivalent to $6.8 \times 10^{-3}\,\mu_B$/FP in these simulation cells) in the global M. This decrease is attributed to the insertion of the FP, which comprises the individual contributions of a single SIA ($-2.93\,\mu_B$) and a single vacancy ($+1.05\,\mu_B$), albeit in a slightly volume-expanded cell. Indeed, in the presence of a SIA (vacancy), the available atomic volume surrounding the defect decreases (increases), thus reducing (raising) the magnetic moments of the atoms enclosing that interstitial (vacant) site. Therefore, the linear reduction in the total M (Fig. 6) can be attributed to the linear accumulation of survived FPs below 0.05 dpa. Beyond 0.05 dpa, however, the number of FPs reaches saturation and interstitial clusters begin to nucleate. Consequently, the change in global M is no longer a linear function of individual FP defects. Therefore, it deviates from the linear decreasing regime and fluctuates around $-0.12\,\mu_B$/atom.[3]

Moreover, it is informative to examine the local magnetic moments of the constituent atoms as a function of dose (FPI number). As shown in Fig. 7, the local magnetic moment of the 1024 atoms (taken from several snapshots of a single CRA trajectory) is plotted with respect to their atomic volumes, computed as the surrounding Voronoi polyhedral cell. Increasing the irradiation dose alters the local environment of the lattice sites, inducing various stress fields around atoms and causing different atomic rearrangements with diverse atomic volumes. Consequently, atoms that undergo a change in their local stress field, in comparison to the post-irradiation conditions, will encounter varying atomic volume and local magnetic moments. To enable a comprehensive understanding of the correlation between atomic volume and local magnetic moments of atoms, we categorized the volume and local moments of atoms into two states: high-volume/high-spin (HV/HS) and low-volume/low-spin (LV/LS). These states are referenced against the atomic volume (11.32 Å) and local magnetic moment ($2.2\,\mu_B$) of a typical iron atom within an undamaged bcc Fe structure. As shown in Fig. 7, the vertical dashed line facilitates the deviation of atomic volume and local magnetic moment of the atoms from those in the undamaged bcc Fe structure. Therefore, the right (left) side of the dashed line corresponds to the HV/HS (LV/LS) state. Atoms with neighboring vacant sites undergo an increase in volume and consequently an increase in local magnetization. Meanwhile, an atom that is in close proximity to interstitial atoms experiences a reduction in its atomic volume and ultimately a decrease in its local magnetization.

As seen in Fig. 7, in the LV/LS region, which refers to the accumulation of SIAs in the damaged structure, it is potentially favorable, both magnetically and structurally, for SIAs to form a locally new crystal structure within the host bcc Fe structure, as we already observed in our simulation [see Fig. S6(b) in [36]].

For example, with an extensive numerical simulation of fictitious amorphous iron at absolute zero temperature, which has similarities to our DFT-CRA evolution at saturation, Krauss and Krey [57] showed a significant connection between the magnitude of the local magnetic moment and the associated local volume of a specific atom in amorphous Fe. Although both these values exhibited considerable variation on a site-to-site basis, their averaged correlation closely aligned with the global volume dependency of local magnetic moments in the antiferromagnetic (AFM) state of face-centered cubic (fcc) Fe, as also computed by Moruzzi *et al.* [58].

Another alternative for the evolution of SIAs, in a massively irradiated structure, is to transform into a C15 Laves phase structure. As demonstrated earlier by Marinica *et al.* [35], the C15 Laves phase in bcc Fe has been established as a stable and immobile framework for the evolution of SIAs. This structural configuration is also marked by significant AFM moments. Such configurations may also emerge during displacement cascade events and has the capability to grow through capturing of further SIAs [35,59,60]. Therefore, C15 structures are assumed to play a critical role in forecasting the radiation-induced evolution of the microstructure in iron-based materials. As previously noted, a limited quantity of extended C15-type interstitial clusters was observed in our DFT-CRA trajectories.

[3]This value can also be obtained by multiplying the total number of survived FPs (∼18) by the global magnetization change per FP (i.e., $6.8 \times 10^{-3}\,\mu_B$).

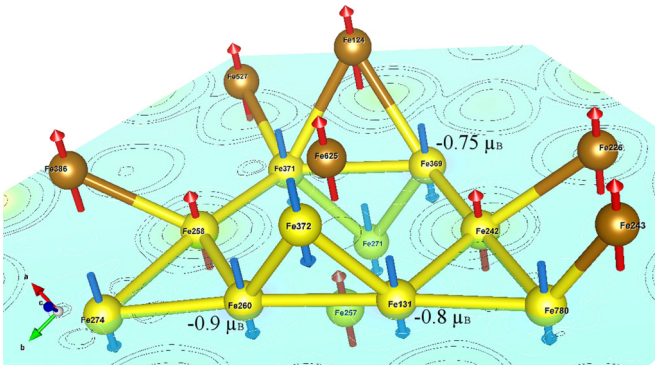

FIG. 8. The structural backbone of a representative C15-type configuration (yellow atoms) formed through DFT-CRA simulation, characterized by a triangular arrangement of di-interstitial and a hexagonal tri-interstitial ring. Blue and red arrows attached to atoms symbolize the corresponding spin-down and spin-up orientations, respectively.

In Fig. 8, an illustrative representation of a prototypical C15-type cluster (yellow color atoms) is provided, with constituent atoms accompanied by their respective site indices. This feature highlights the core framework of the C15-type structure, emerging from the DFT-CRA simulation, which comprises both a triangular configuration of a di-interstitial and a hexagonal tri-interstitial ring formation. Notably, within this example cluster, specific atoms like Fe131 or Fe260 exhibit AFM orientation, quantified at -0.8 and $-0.9\,\mu_B$, respectively. A comparison to a conventional FM bcc Fe atom emphasizes this difference. Further examination of the projected density of states (DOS) and integrated DOS of Fe131, compared to a pristine lattice atom, highlights the influence of neighboring atoms within the cluster (refer to Fig. 9). As shown, in a damaged structure where lattice deformation occurs, the interaction with surrounding atoms induces a separation between t_{2g} and e_g d-orbitals,[4] prompting a reconfiguration of d-orbitals [61]. Consequently, a deviation from the initial majority and minority spin populations, depicted in Fig. 9(b), near and at the Fermi level, results in distinct spin orientations and local magnetic moments for the displaced atoms.

Finally, we investigate the interplay between swelling and global M in the damaged Fe structure using different types of relaxation conditions. Initially, we traced the radiation-induced swelling from ionic relaxation conditions [Fig. 5(a)]. It is noteworthy that these calculations might overestimate the radiation-induced swelling due to the assumption of a constant cell volume. To accurately account for the impact of volume relaxation, we initiated an exploration of magnetovolume instability in a standard pristine FM bcc Fe cell. By progressively expanding the cell volume while maintaining ion positions fixed, we computed the per-atom change in total M within an electronically converged structure. This

[4]Generally, the d-orbitals can be categorized into two distinct sets referred to as t_{2g} (comprising d_{xy}, d_{xz}, and d_{yz}) and e_g (encompassing $d_{x^2-y^2}$ and d_{z^2}) orbitals. However, within specific crystal field environments, these five d-orbitals undergo division into varied configurations, contingent upon the symmetry characteristics of the neighboring d-orbital electrons [61].

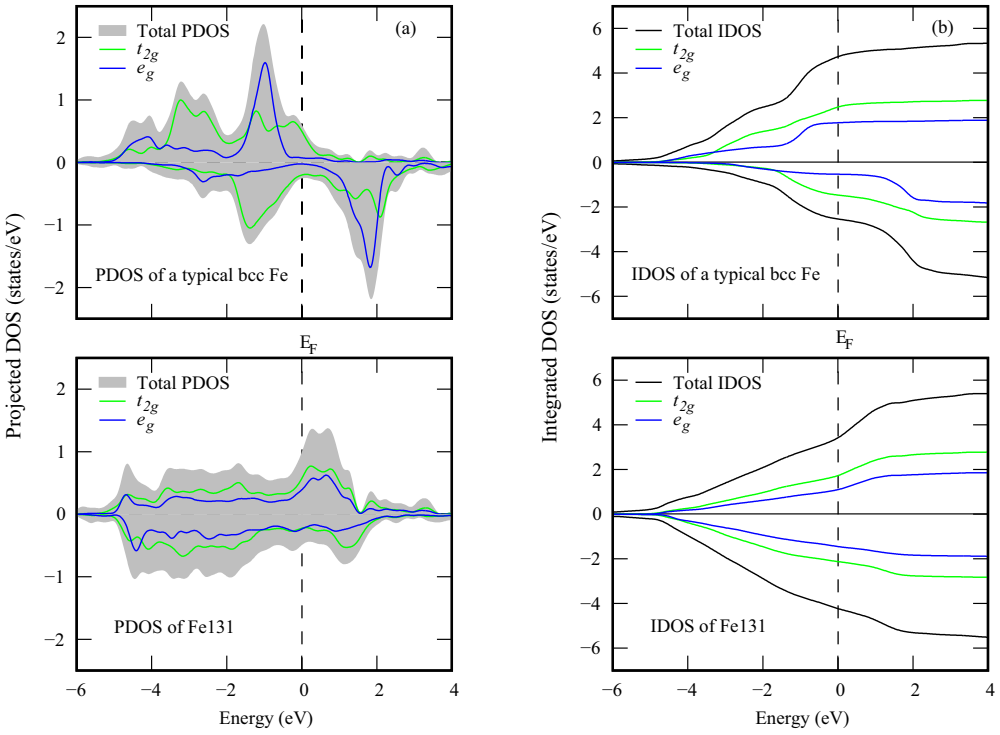

FIG. 9. Comparison of the (a) projected density of states (PDOS) and (b) integrated density of states (IDOS) for the Fe131 atom in the C15-type structure (bottom panels) with that of a typical Fe atom in a standard bcc structure (top panels). The dashed lines show the Fermi energy levels, set at $E_F = 0$.

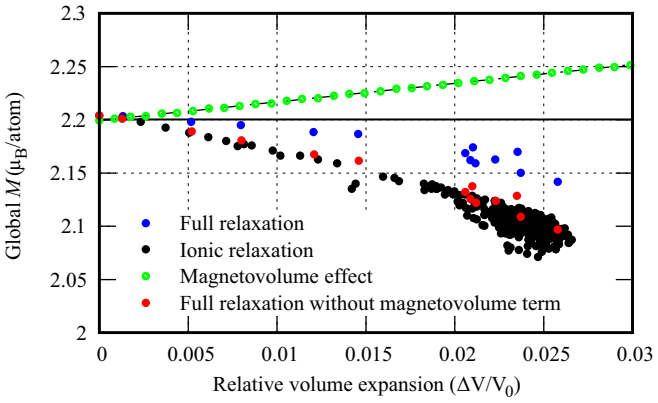

FIG. 10. Total magnetization per atom with relative volume expansion. The results of full relaxation calculation with and without magnetovolume effect are shown with blue- and red-filled circles, respectively.

insight allows us to correct the estimated swelling, by introducing the magnetovolume term to the M change obtained from ionic relaxation calculations. Conversely, by subtracting the magnetovolume term from full relaxation computation results, one can replicate the outcomes of ionic relaxation for predicting swelling. The effectiveness of this approach is evident from Fig. 10, where removing the magnetovolume term from full relaxation calculation results (blue-filled circles) aligns the global M shifts (red-filled circles) with data points extracted from ionic relaxation calculations (black-filled circles). This correction mechanism offers an avenue for fast ionic relaxation calculations while explicitly accounting for radiation-induced swelling through correction with the magnetovolume effect.

Moreover, Fig. 10 demonstrates that up to a relative volume change of 2%, isolated defects accumulate linearly, with the count of FPI nearly matching the number of survived isolated point defects. As the relative volume change surpasses $\Delta V/V_0 > 2\%$, the clustering of SIAs into larger features, e.g., C15 Laves phase, signals a transition from a linear point defect buildup to a stable pattern of larger and larger clusters as the irradiation dose escalates. This progression of microstructure evolution highlights the intricate interplay between volume changes and defect clustering phenomena.

IV. CONCLUSION

In summary, we have introduced a first-principles approach to investigate microstructure evolution. Through the utilization of the CRA model, we explored the radiation-induced microstructure evolution and defect clustering in heavily irradiated bcc Fe. The validation of EAM-CRA results against DFT-CRA predictions shows the level of accuracy to which the EAM methodology is reliable and for which quantities. Additionally, our study addressed magnetization changes within the evolving microstructure. While the EAM-CRA model holds promise for investigating microstructure evolution in large supercells, the DFT-CRA excellently provides electronic structure information for exploring effects such as magnetization charge evolution and holds great promise for studying systems with complex chemistry.

Analyzing a 1024-atom supercell highlighted the minor differences between uniform and localized SIA implantation distributions, whereas larger supercells necessitate the use of localized SIA distribution for modeling of low-energy damage conditions. We found qualitative agreement between EAM potentials and DFT methodology for several properties. However, the EAM-M07 potential seemed to overstabilize the transformation of large SIA clusters into C15 Laves phase structures in a highly defected bcc Fe lattice.

Moreover, our investigation revealed a two-stage microstructure evolution under CRA conditions: initial linear accumulation of isolated point defects followed by steady-state clustering, irrespective of thermally activated diffusion, as reported in experimental observations.

Importantly, our study demonstrated the usefulness of access to electronic structure effects through the correlation of magnetovolume effects in the DFT-CRA ionic relaxation calculations to reproduce precise microstructure transformation observed in full relaxation conditions.

Finally, our integrated approach merges first-principles theory and innovative modeling to elucidate radiation-induced microstructure evolution mechanisms and can be applied to chemically complex systems which are not accessible via interatomic potential-based simulations. These findings enhance our comprehension of these processes, offering insights for more efficient materials science and radiation damage studies.

ACKNOWLEDGMENTS

The authors are grateful for insightful discussions with Sergei Dudarev and Peter Derlet. This work was conducted with financial support from the Swedish Foundation for Strategic Research (SSF) under Grant No. ARC19-0043 (the SUNRISE center) and Swedish Research Council (VR) within projects 2017-06458 and 2019-04156. It was joined to the framework of the EUROfusion Consortium, funded by the European Union via the Euratom Research and Training Programme (Grant Agreement No. 101052200—EUROfusion). The work was also partly funded by the Euratom Research and Training Programme 2019–2020 under Grant Agreements No. 755039 (M4F project) and No. 740415 (IL TROVATORE project). The views and opinions expressed are, however, those of the authors only and do not necessarily reflect those of the European Union or the European Commission. Neither the European Union nor the European Commission can be held responsible for them. The computational resources were provided by the Swedish National Infrastructure for Computing (SNIC; PDC at KTH and NSC at LiU) and by the CINECA HPC Center in Italy.

APPENDIX A: THE FZR CRITERION

Employing the DFT approach, we established the FZR criterion within a bcc Fe structure. The corresponding supercell encompassed $5 \times 5 \times 5$ copies of a bcc Fe unit cell, comprising 250 lattice sites. To ensure precision, a cut-off energy of 350 eV was employed, accompanied by a $6 \times 6 \times 6\,k$-point sampling of the Brillouin zone. Both lattice parameter

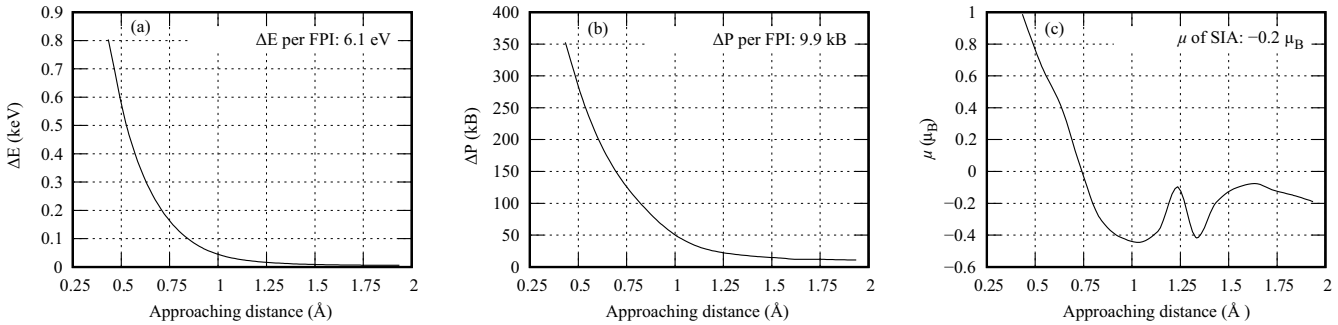

FIG. 11. The change in (a) total energy, (b) global pressure, and (c) local magnetic moment of a SIA as a function of the approaching distance of atoms forming a ⟨110⟩-dumbbell.

optimization and electronic structure calculation were executed using the conjugate gradient algorithm.

Following a complete relaxation calculation, a FP was introduced into the supercell, comprising a vacancy at the origin and an interstitial at the midlattice site. In essence, this led to the establishment of a ⟨110⟩-dumbbell configuration. Initially, the distance between the atoms constituting the dumbbell configuration was approximately 2 Å, while the distance between the vacancy and the center of mass of the ⟨110⟩-dumbbell measured 12.26 Å. This substantial separation ensured the absence of interaction or recombination between the SIAs and vacancy.

The calculated formation energy of the FP, approximately 6.1 eV, is in complete agreement with findings from other DFT studies [62,63]. Furthermore, the introduction of a single FP leads to changes in global pressure and total magnetization of the system by approximately 9.9 kB and $-1.7\,\mu_B$, respectively. In addition, the local magnetic moments of the SIAs equally decrease to $-0.2\,\mu_B$.

To investigate the variations in total energy and hydrostatic pressure changes as well as local magnetic moment of SIAs, we incrementally reduced the distance between the two constituent atoms of a ⟨110⟩-dumbbell. Subsequently, self-consistent electronic calculations were conducted while maintaining the positions of other ions constant.

In Fig. 11, we analyzed the interplay of total energy and hydrostatic pressure changes as well as the local magnetic moment (μ) of SIAs concerning varying interatomic distances. Notably, at an interatomic separation of approximately 0.7 Å, the local magnetic moment of SIAs shifts to a positive value while the total energy change becomes remarkably pronounced, surpassing the FP formation energy by a factor of 33. This shift is also evident in the hydrostatic pressure, displaying an order of magnitude increase compared to FP-induced pressure. These findings underscore the substantial influence of interatomic proximity on SIA properties and system stability.

In summary, establishing a virtual restricted region encompassing lattice atoms finds justification through a proportional fractional delineation based on the equilibrium interatomic separation. Notably, this virtual threshold is defined to circumvent the incorporation of atoms at distances closer than this critical value, i.e., 0.7 Å, within the model. Indeed, this precaution is rooted in recognizing that the local magnetic moment does not attain its negative value under the perturbed circumstances; it assumes an unfavorable disposition. The designated distance safeguards against introducing nonphysical elements into the CRA model, mitigating the distortions arising from undue atom proximity.

APPENDIX B: SPATIAL DISTRIBUTION FUNCTIONS

1. Uniform spatial continuous distribution function

For a uniform atom displacement, one can use a continuous distribution function. By definition, a continuous random variable x has a uniform distribution over an interval $[a, b]$, shown as $x \in$ uniform $[a, b]$, if its probability density function (PDF) is given by [64,65]

$$f(x) = \begin{cases} \frac{1}{b-a}, & a \leqslant x \leqslant b \\ 0, & \text{otherwise} \end{cases} \tag{B1}$$

Using this function will uniformly produce a random number within the interval $[a, b]$ and its expected value (i.e., mean displacement) is given by

$$EX = \frac{b-a}{2}. \tag{B2}$$

For example, the mean value of the atom displacement with the uniform distribution function in a box with side length of $8 \times a_0$ ($a_0 = 2.831$ Å) is 11.32 Å.

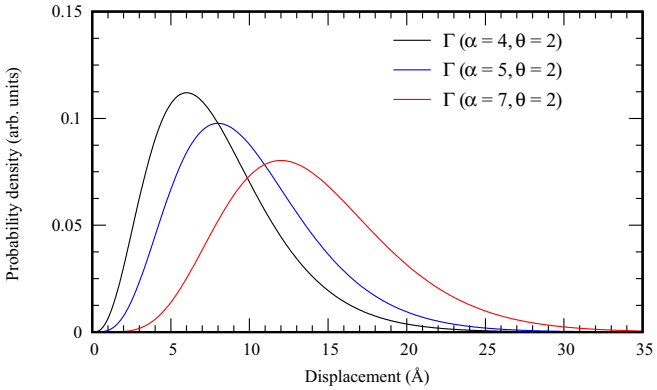

FIG. 12. Plot of PDFs of standard $\Gamma(\alpha,\theta)$ distribution function for various shape and scale parameters.

2. Localized spatial continuous distribution function

For a localized atom displacement, we applied the gamma distribution function. The gamma distribution function is a widely used distribution due to its relation to exponential and normal distribution functions. The standard gamma distribution, $\Gamma(\alpha,\theta)$, has two free parameters, labeled as α and θ, and its PDF is given as [65]

$$f(x;\alpha,\theta) = \frac{x^{\alpha-1}e^{-x/\theta}}{\Gamma(\alpha)\theta^{\alpha}}, \quad 0 < x < \infty. \tag{B3}$$

The parameters α and θ are shape and scale parameters, respectively. $\Gamma(\alpha)$ is also the gamma function [65]. As shown in Fig. 12, the PDFs of a standard gamma distribution are plotted for different α and θ parameters for comparison.

The expected value (i.e., mean displacement) of the $\Gamma(\alpha,\theta)$ is given by the following formula.

$$EX = \alpha \times \theta. \tag{B4}$$

Gamma distributions are used to model non-negative quantities skewed to the right. In other words, they can often be applied to model random times, weights, and lengths. In our study, we used two gamma distribution functions, $\Gamma(4,2)$ and $\Gamma(5,2)$, with mean displacements of 8 and 10 Å, respectively.

[1] K. L. Murty and I. Charit, Structural materials for Gen-IV nuclear reactors: Challenges and opportunities, J. Nucl. Mater. **383**, 189 (2008).

[2] S. J. Zinkle, Radiation-induced effects on microstructure, Compr. Nucl. Mater. **1**, 65 (2012).

[3] A. Aitkaliyeva, L. He, H. Wen, B. Miller, X. M. Bai, and T. Allen, Irradiation effects in Generation IV nuclear reactor materials, in *Structural Materials for Generation IV Nuclear Reactors*, edited by P. Yvon (Elsevier, New York, 2017), p. 253.

[4] C. Cawthorne and E. J. Fulton, Voids in irradiated stainless steel, Nature (London) **216**, 575 (1967).

[5] P.-W. Ma, D. R. Mason, and S. L. Dudarev, Multiscale analysis of dislocation loops and voids in tungsten, Phys. Rev. Mater. **4**, 103609 (2020).

[6] A. J. Ardell and P. Bellon, Radiation-induced solute segregation in metallic alloys, Curr. Opin. Solid State Mater. Sci. **20**, 115 (2016).

[7] D. Kaoumi, J. Adamson, and M. Kirk, Microstructure evolution of two model ferritic/martensitic steels under in situ ion irradiation at low doses (0–2 dpa), J. Nucl. Mater. **445**, 12 (2014).

[8] M. Hernández-Mayoral and M. J. Caturla, Microstructure evolution of irradiated structural materials in nuclear power plants, in *Understanding and Mitigating Ageing in Nuclear Power Plants*, edited by P. G. Tipping (Woodhead Publishing, Cambridge, UK, 2010), p. 189.

[9] L. Koch, F. Granberg, T. Brink, D. Utt, K. Albe, F. Djurabekova, and K. Nordlund, Local segregation versus irradiation effects in high-entropy alloys: Steady-state conditions in a driven system, J. Appl. Phys. **122**, 105106 (2017).

[10] S. M. Bruemmer, E. P. Simonen, P. M. Scott, P. L. Andresen, G. S. Was, and J. L. Nelson, Radiation-induced material changes and susceptibility to intergranular failure of light-water-reactor core internals, J. Nucl. Mater. **274**, 299 (1999).

[11] W. Liu, Y. Ji, P. Tan, H. Zang, C. He, D. Yun, C. Zhang, and Z. Yang, Irradiation induced microstructure evolution in nanostructured materials: A review, Materials **9**, 105 (2016).

[12] C. S. Deo, E. Y. Chen, and R. Dingeville, Atomistic modeling of radiation damage in crystalline materials, Model. Simul. Mater. Sci. Eng. **30**, 023001 (2021).

[13] Y. Li, S. Hu, X. Sun, and M. Stan, A review: Applications of the phase field method in predicting microstructure and property evolution of irradiated nuclear materials, npj Comput. Mater. **3**, 16 (2017).

[14] J.-P. Crocombette and D. Ghaleb, Molecular dynamics modeling of irradiation damage in pure and uranium-doped zircon, J. Nucl. Mater. **295**, 167 (2001).

[15] S. L. Dudarev, Density functional theory models for radiation damage, Annu. Rev. Mater. Res. **43**, 35 (2013).

[16] L. Malerba *et al.*, Multiscale modelling for fusion and fission materials: The M4F Project, Nucl. Mater. Energy **29**, 101051 (2021).

[17] M. J. Caturla, A. Gras Martı, J. J. Jiménez-Rodrıguez, J.-C. Jiménez Saez, and M.-C. Pérez-Martın, Molecular dynamics simulations of energy deposition in solids, in *Advances in Quantum Chemistry* (Academic, New York, 2004), Vol. 45, p. 79.

[18] C. Domain, C. S. Becquart, and L. Malerba, Simulation of radiation damage in Fe alloys: An object kinetic Monte Carlo approach, J. Nucl. Mater. **335**, 121 (2004).

[19] D. J. Bacon and Yu. N. Osetsky, Multiscale modelling of radiation damage in metals: From defect generation to material properties, Mater. Sci. Eng.: A **365**, 46 (2004).

[20] K. Nordlund *et al.*, Improving atomic displacement and replacement calculations with physically realistic damage models, Nat. Commun. **9**, 1084 (2018).

[21] G. H. Kinchin and R. S. Pease, The displacement of atoms in solids by radiation, Rep. Prog. Phys. **18**, 1 (1955).

[22] M. J. Norgett, M. T. Robinson, and I. M. Torrens, A proposed method of calculating displacement dose rates, Nucl. Eng. Des. **33**, 50 (1975).

[23] D. R. Mason, A. E. Sand, and S. L. Dudarev, Atomistic-object kinetic Monte Carlo simulations of irradiation damage in tungsten, Model. Simul. Mater. Sci. Eng. **27**, 055003 (2019).

[24] L. Casillas-Trujillo, A. S. Ervin, L. Xu, A. Barashev, and H. Xu, Dynamics of Interaction between dislocations and point defects in bcc iron, Phys. Rev. Mater. **2**, 103604 (2018).

[25] F. Granberg, J. Byggmästar, and K. Nordlund, Molecular dynamics simulations of high-dose damage production and defect evolution in tungsten, J. Nucl. Mater. **556**, 153158 (2021).

[26] P. M. Derlet and S. L. Dudarev, Microscopic structure of a heavily irradiated material, Phys. Rev. Mater. **4**, 023605 (2020).

[27] F. Granberg, J. Byggmästar, and K. Nordlund, Defect accumulation and evolution during prolonged irradiation of Fe and FeCr alloys, J. Nucl. Mater. **528**, 151843 (2020).

[28] Y. Limoge, A. Rahman, H. Hsieh, and S. Yip, Computer simulation studies of radiation induced amorphization, J. Non-Cryst. Solids **99**, 75 (1988).

[29] A. Chartier and M.-C. Marinica, Rearrangement of interstitial defects in alpha-Fe under extreme condition, Acta Mater. **180**, 141 (2019).

[30] M. J. Sabochick and N. Q. Lam, Radiation-induced amorphization of ordered intermetallic compounds CuTi, $CuTi_2$ and Cu_4Ti_3: A molecular-dynamics study, Phys. Rev. B **43**, 5243 (1991).

[31] S. Aidhy, P. C. Millett, T. Desai, D. Wolf, and S. R. Phillpot, Kinetically evolving irradiation-induced point defect clusters in UO_2 by molecular dynamics simulation, Phys. Rev. B **80**, 104107 (2009).

[32] C. Jiang, M.-J. Zheng, D. Morgan, and I. Szlufarska, Amorphization driven by defect-induced mechanical instability, Phys. Rev. Lett. **111**, 155501 (2013).

[33] L. Malerba *et al.*, Comparison of empirical interatomic potentials for iron applied to radiation damage studies, J. Nucl. Mater. **406**, 19 (2010).

[34] M. I. Mendelev, S. Han, D. J. Srolovitz, G. J. Ackland, D. Y. Sun, and M. Asta, Development of new interatomic potentials appropriate for crystalline and liquid iron, Philos. Mag. **83**, 3977 (2003).

[35] M.-C. Marinica, F. Willaime, and J.-P. Crocombette, Irradiation-induced formation of nanocrystallites with C15 Laves phase structure in bcc iron, Phys. Rev. Lett. **108**, 025501 (2012).

[36] See Supplemental Material at http://link.aps.org/supplemental/10.1103/PhysRevMaterials.7.123604 for predictive capabilities of EAM-CRA methodologies across varied supercell sizes; comprehensive comparisons of defect populations and their cluster sizes using diverse methodologies and supercell sizes; different DFT-CRA calculation methods in comparing swelling anticipation against estimated values through $\Delta P/B$ ratio and affirming the reliability of ionic relaxation calculations; DFT-CRA predictions with experimentally measured radiation-induced changes in lattice constants and crystalline structures; irradiation-induced changes in stress tensor components; and the intricacies of irradiation-induced changes in local magnetization and charge density around point defects. It also contains Refs. [26,55,62,63].

[37] K. Nordlund, N. Runeberg, and D. Sundholm, Repulsive interatomic potentials calculated using Hartree-Fock and density-functional theory methods, Nucl. Instrum. Methods Phys. Res., Sect. B **132**, 45 (1997).

[38] P. E. Blöchl, Projector augmented-wave method, Phys. Rev. B **50**, 17953 (1994).

[39] A. Stukowski, Visualization and analysis of atomistic simulation data with OVITO–the open visualization tool, Model. Simul. Mater. Sci. Eng. **18**, 015012 (2009).

[40] C. Björkas and K. Nordlund, Comparative study of cascade damage in Fe simulated with recent potentials, Nucl. Instrum. Methods Phys. Res. Sect. B **259**, 853 (2007).

[41] D. Terentyev, C. Lagerstedt, P. Olsson, K. Nordlund, J. Wallenius, C. S. Becquart, and L. Malerba, Effect of the interatomic potential on the features of displacement cascades in α-Fe: A molecular dynamics study, J. Nucl. Mater. **351**, 65 (2006).

[42] P. M. Larsen, S. Schmidt, and J. Schiøtz, Robust structural identification via polyhedral template matching, Modell. Simul. Mater. Sci. Eng. **24**, 055007 (2016).

[43] G. Sun, J. Kürti, P. Rajczy, M. Kertesz, J. Hafner, and G. Kresse, Performance of the Vienna ab initio simulation package (VASP) in chemical applications, J. Mol. Struct.: THEOCHEM **624**, 37 (2003).

[44] T. Harte, G. D. Bruce, J. Keeling, and D. Cassettari, Conjugate gradient minimisation approach to generating holographic traps for ultracold atoms, Opt. Express **22**, 26548 (2014).

[45] J. P. Perdew, K. Burke, and M. Ernzerhof, Generalized gradient spproximation made dimple, Phys. Rev. Lett. **77**, 3865 (1996).

[46] J. P. Perdew, Generalized gradient approximations for exchange and correlation: A look backward and forward, Phys. B (Amsterdam, Neth.) **172**, 1 (1991).

[47] D. V. Schroeder, *An Introduction to Thermal Physics* (Oxford University Press, New York, 2021), Vol. 27.

[48] K. Momma and F. Izumi, VESTA: A three-dimensional visualization system for electronic and structural analysis, J. Appl. Crystallogr. **41**, 653 (2008).

[49] H. Hasegawa, A theory of magneto-volume effects of itinerant-electron magnets. I. Spontaneous volume magnetostriction, J. Phys. C: Solid State Phys. **14**, 2793 (1981).

[50] A. P. Thompson *et al.*, LAMMPS - a flexible simulation tool for particle-based materials modeling at the atomic, meso, and continuum scales, Comput. Phys. Commun. **271**, 108171 (2022).

[51] J. Byggmästar, F. Granberg, and K. Nordlund, Effects of the short-range repulsive potential on cascade damage in iron, J. Nucl. Mater. **508**, 530 (2018).

[52] X. Jin, A. Boulle, A. Chartier, J.-P. Crocombette, and A. Debelle, Analysis of strain and disordering kinetics based on combined RBS-channeling and x-ray diffraction atomic-scale modelling, Acta Mater. **201**, 63 (2020).

[53] A. Chartier, C. Onofri, L. Van Brutzel, C. Sabathier, O. Dorosh, and J. Jagielski, Early stages of irradiation induced dislocations in urania, Appl. Phys. Lett. **109**, 181902 (2016).

[54] L. Dézerald, M.-C. Marinica, L. Ventelon, D. Rodney, and F. Willaime, Stability of self-interstitial clusters with C15 Laves phase structure in iron, J. Nucl. Mater. **449**, 219 (2014).

[55] K. Papamihail, K. Mergia, F. Ott, Y. Serruys, Th. Speliotis, G. Apostolopoulos, and S. Messoloras, Fe^+ ion irradiation induced changes in structural and magnetic properties of iron films, Nucl. Mater. Energy **9**, 459 (2016).

[56] K. Papamihail, K. Mergia, F. Ott, Y. Serruys, Th. Speliotis, G. Apostolopoulos, and S. Messoloras, Magnetic effects induced by self-ion irradiation of Fe films, Phys. Rev. B **93**, 100404(R) (2016).

[57] U. Krauss and U. Krey, Local magneto-volume effect in amorphous iron, J. Magn. Magn. Mater. **98**, L1 (1991).

[58] V. L. Moruzzi, P. M. Marcus, and J. Kübler, Magnetovolume instabilities and ferromagnetism versus antiferromagnetism in bulk fcc iron and manganese, Phys. Rev. B **39**, 6957 (1989).

[59] D. J. Bacon, F. Gao, and Yu. N. Osetsky, The primary damage state in fcc, bcc and hcp metals as seen in molecular dynamics simulations, J. Nucl. Mater. **276**, 1 (2000).

[60] F. Gao, D. J. Bacon, Yu. N. Osetsky, P. E. J. Flewitt, and T. A. Lewis, Properties and evolution of sessile interstitial clusters produced by displacement cascades in α-iron, J. Nucl. Mater. **276**, 213 (2000).

[61] S. Blundell, *Magnetism in Condensed Matter* (Oxford University Press, Oxford, 2001), p. 45.

[62] P. Olsson, C. Domain, and J. Wallenius, *Ab initio* study of Cr interactions with point defects in bcc Fe, Phys. Rev. B **75**, 014110 (2007).

[63] P. Olsson, C. S. Becquart, and C. Domain, *Ab initio* threshold displacement energies in iron, Mater. Res. Lett. **4**, 219 (2016).

[64] F. M. Dekking, C. Kraaikamp, H. P. Lopuhaä, and L. E. Meester, *A Modern Introduction to Probability and Statistics: Understanding Why and How* (Springer, London, 2010).

[65] J. Proakis, Probability, random variables and stochastic processes, IEEE Trans. Acoust., Speech, Signal Process. **33**, 1637 (1985).